Nanoscale

ROYAL SOCIETY OF CHEMISTRY

PAPER

View Article Online
View Journal | View Issue

Cite this: *Nanoscale*, 2021, **13**, 1311

Phase change material based hot electron photodetection

Sandeep Kumar Chamoli, [a,b,c] Gopal Verma, *[a] Subhash C. Singh *[a,c] and Chunlei Guo*[c]

We introduce a phase change material (PCM) based metal–dielectric–metal (MDM) cavity of gold (Au)–antimony trisulfide (Sb_2S_3)–Au as a hot electron photodetector (HEPD). Sb_2S_3 shows significant contrast in the bandgap (E_g) upon phase transition from the crystalline (Cry) (E_g = 2.01 eV) to the amorphous (Amp) (E_g = 1.72 eV) phase and forms the lowest Schottky barrier with Au in its Amp phase compared to conventional semiconductors such as Si, MoS_2, and TiO_2. The proposed HEPD is tunable for absorption and responsivity in the spectral range of 720 nm < λ < 1250 nm for the Cry phase and 604 nm < λ < 3542 nm for the Amp phase. The single resonance cavity and thus the sensitivity of the designed HEPD device can be changed to the double resonance cavity *via* the Cry to Amp phase transition. The maximum predicted responsivities for the single and double cavities are 20 and 24 mA W^{-1}, respectively, at 950 nm and 1050 nm wavelengths which is the highest among all previously proposed planar HEPD devices. An anti-symmetric resonance mode at a higher wavelength is observed in the double cavity with 100% absorption. Owing to a high index of Sb_2S_3, an ultrathin ~40 nm (~λ/15) MDM cavity supports a critical light coupling to achieve high-efficiency HEPDs. Furthermore, a reversible and ultrafast (~70 ns) Cry to Amp phase transition of Sb_2S_3 makes it suitable for many tunable photonics applications ranging from the visible to near-infrared region. Finally, we have introduced a novel scheme to switch between the single and double cavity by exploiting a semiconductor to metal phase transition in a PCM called VO_2. The integration of VO_2 as a coupling medium in the double cavity has increased the responsivity up to 50% upon phase transition to the metal phase. The proposed design can be used in optical filters, optical switches, ultrathin broad or narrow band solar absorbers, and other energy applications such as water splitting.

Received 7th September 2020,
Accepted 1st December 2020

DOI: 10.1039/d0nr06456d

rsc.li/nanoscale

Introduction

Photovoltaic techniques provide a platform for the generation of electric power through photon absorption. Photon absorption by the MDM junction results in the generation of excited electron–hole pairs.[1] In the visible and NIR regions, the e^- mean free path can be larger than the metal film thickness of an MDM cavity that could allow the propagation of electrons over a long distance without decreasing their energy through scattering and collisional losses. If e^- is carrying higher energy to overcome the band offset between metal–dielectric interfaces, it can contribute to the current.[2] The concept of hot e^- is mostly used to determine the Schottky barrier height (ϕ_b) at a metal–dielectric interface. Recently, hot electron generation (HEG) has been extensively used in many research areas including photodetection,[3,4] photovoltaics,[5] optical modulation,[6] surface imaging,[7] and photocatalysis.[8] The injection of hot electrons from the metal to the conduction band of an adjacent semiconductor or insulator by crossing the Schottky barrier at the interface allows the detection of photons of energy less than the bandgap, thus increasing the detection bandwidth.

Recently, several designs of HEPDs have been proposed and/or fabricated using sub-wavelength plasmonic nanostructures including nanowires,[9] gratings,[10] nanoparticles[11,12] nanodiodes,[13,14] and metamaterials.[15] These HEPDs demonstrated close-to-perfect absorption of light in narrow or broadband spectral regions.[16,17] However, the fabrication of sub-wavelength nanostructures in the previous HEPDs required state-of-the-art nanofabrication systems and multi-step complex and precise processing that imposed a limitation on their scalability for practical applications. In contrast to plas-

[a]*The Guo Photonics Laboratory, State Key Laboratory of Applied Optics, Changchun Institute of Optics, Fine Mechanics and Physics, Chinese Academy of Sciences, Changchun 130033, China. E-mail: gopal@ciomp.ac.cn*
[b]*University of Chinese Academy of Science, Beijing 100039, China. E-mail: chamolisandeep28@mails.ucas.ac.cn*
[c]*The Institute of Optics, University of Rochester, Rochester, New York 14627, USA. E-mail: ssingh49@ur.rochester.edu, guo@optics.rochester.edu*

monic nanostructures, multilayered structures are made of several layers of metals and dielectrics or semiconductors with or without any particular patterns.[18,19] Very recently, planar MDM based hot electron photodetectors have been theoretically and experimentally explored.[4,18–20] Optical absorption in planar HEPDs can be increased *via* increasing the thickness of the metal layer, but the generated hot electrons must reach the metal/dielectric interface before thermal relaxation. This restricts the use of thicker metal films in planar HEPDs. A high optical absorption with a thin metal film can be achieved by employing a Fabry–Perot (FP) cavity or optical Tamm Plasmon (TP)[18,19] systems.

Generally, in MDM based HEPDs, the electromagnetic (EM) radiation strikes on the top metal film generating hot carriers (hot e^- or holes). Due to the high kinetic energy, they cross ϕ_b and get injected into the semiconductor or insulator layer and finally contribute to the photocurrent. This process introduces a technique for the detection of photon energy less than E_g and higher than ϕ_b ($\phi_b < h\nu < E_g$). For Sb_2S_3, the values of ϕ_b (at the Au–Sb_2S_3 interface) and E_g in the Cry and Amp phases are (1 eV, 1.72 eV) and (0.35 eV, 2.01 eV), respectively. This offers broadband and tunable hot electron-based photodetection by tuning the phase of Sb_2S_3. Owing to its large bandgap, high absorption coefficient, environment friendliness, and large abundance, Sb_2S_3 has recently emerged as a reliable phase change material. Materials such as cadmium telluride (CdTe), Cu (In, Ga), Se_2 (CIGS), and perovskites (organic–inorganic metal halides *e.g.* $CH_3NH_3PbI_3$) are preferred for photothermal[20] and photovoltaic[21] based photodetection with amazing detection capability in a broad spectral range. However, rare Earth elements In and Te have limited availability on the Earth, and Cd and Pb are toxic. This leads to the crucial demand for photodetector materials made of Earth-abundant, nontoxic elements, and cost-effective for the scalable process. Moreover, the spectral absorption bandwidth for a conventional PV-based photodetector material is limited by its bandgap; thus, the device generally has a narrow operational bandwidth. Nanoscale periodic structures, such as antennas, are required to increase the sensitivity of a PV-based photodetector beyond its band edge.[21] Fabrication of nanoscale periodic structures, however, demands multi-step, costly, and time-consuming methods that increase the cost of the device.

In this letter, we have introduced a planar HEPD device based on a PCM in the MDM cavity configuration. The device can dynamically tune its photoresponse from the visible to the NIR region. The PCM provides a dynamic response from the cavity due to the significant contrast in the index and absorption between its Cry and Amp phases. Depending on the critical light coupling parameters such as cavity, thickness, and refractive index, multiple broad or narrow absorption bands are observed from the visible to NIR region. The thickness of the top metal film is ~15 nm to attain the maximum photon absorption and hot e^- collection simultaneously. The ϕ_b values at the Au–Sb_2S_3 interface in the Cry phase and the Amp phase are 1 eV and 0.35 eV, respectively. The spectral range for the designed HEG based photodetector is 604–3542 nm (ultra-broadband of 2938 nm) including both the Cry and Amp phases. This is due to the significant contrast in ϕ_b between the two phases. Therefore, the proposed work provides a PCM based platform for dynamic control over photoresponse ranging from the visible to NIR region. Finally, we have designed a hybrid double cavity consisting of the Cry and Amp phases of Sb_2S_3, so the double cavity can take four possible combinations as follows: Amp–Amp, Amp–Cry, Cry–Cry, and Cry–Amp. We chose the Amp–Amp double cavity for our calculation. We have realized a significant increment in the responsivity from 20 mA W^{-1} in the single cavity to 24.58 mA W^{-1} in the double cavity. An antisymmetric resonance mode at a higher wavelength and a symmetric mode at a lower wavelength are observed in the hybrid double cavity. Finally, we introduced another PCM, VO_2, in the double cavity. The metal to semiconductor phase transition in the VO_2 layer plays an important role in coupling the top and bottom cavities. The estimated responsivity has shown 50% enhancement in the VO_2-metal phase. The present work provides a new route to switch the dual to single cavity upon a fast phase change in PCMs.

Results and discussion

A schematic of the proposed single cavity PCM-HEPD device is shown in Fig. 1. The structure is as follows: Au–Sb_2S_3–Au. The thicknesses of the top Au and Sb_2S_3 layers are t and h, respectively, and have been optimized for cavity modes. Au is chosen due to its lowest ϕ_b with Sb_2S_3 and higher stability over other metals. Sb_2S_3 is a PCM that can undergo a reversible transition from its Cry to Amp phase upon opto-thermal or electro-thermal heating at temperatures higher than 573 K (Cry phase) and 801 K (Amp phase). It possesses many attractive properties, namely, an ultrafast switching speed of ~70 ns and a large bandgap. The large bandgap of Sb_2S_3 makes it an ideal candidate for many tunable photonics applications in the visible spectral range as it shows relatively low losses.[22,23] Also, both states are stable at room temperature. The Cry phase of

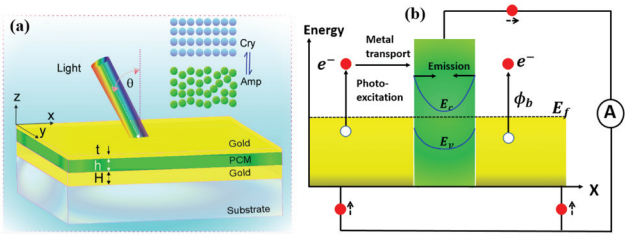

Fig. 1 (a) Schematic of the proposed PCM-HEPD. (b) Energy band diagram at equilibrium (no biasing); E_f and ϕ_b are the Fermi level and Schottky barrier height, respectively. In the Cry phase ϕ_b = 1 eV and in the Amp phase ϕ_b = 0.35 eV, the diffusion length of the generated hot electrons at the Au–Sb_2S_3 interface is ~30 nm. Hot e^- harvesting involves three steps: (1) photoexcitation or generation of hot e^-, (2) transport of hot e^- to the interface and finally (3) emission into Sb_2S_3.

Sb_2S_3 has a higher refractive index than the Amp phase reaching a maximum difference of $\Delta n \sim 1$ at 614 nm. On the other hand, its extinction coefficient is negligible for wavelengths $\lambda >$ 605 nm for the Cry phase and $\lambda >$ 714 nm for the Amp phase. In general, the Amp phase is treated as a covalently bonded random network. On the other hand, the Cry phase is a highly periodic structure (see the inset of Fig. 1(a)).

The transfer matrix method (TMM) approach is used for all the simulation work in FDTD Lumerical. A light beam in the wavelength range 400 to 1200 nm illuminates the structure in the downward Z-direction. The refractive index data for Sb_2S_3 from 400 nm to 800 nm are taken from a report and extrapolated till 1200 nm.[22] So we limit our calculations in the wavelength ranging from 400 nm to 1200 nm.

Fig. 1(b) shows the energy band diagram of the proposed PCM based HEPD. E_f is the Fermi energy of Au and Sb_2S_3 in equilibrium (no bias). E_c and E_v are the minima of the conduction band (CB) edge and the maxima of the valence band (VB) edge. The potential barrier, $\phi_b = W - \chi$, depends on the work function of Au ($W \sim 5.1$ eV) and the electron affinity of Sb_2S_3 ($\chi \sim 4.76$ eV in the Cry phase and 4 eV in the Amp phase). Usually, the theoretical prediction for ϕ_b deviates from the experimental results due to the presence of surface defects in the actual devices. Additionally, ϕ_b at the Au–Sb_2S_3 interface is smaller over conventionally used hot e^- Schottky barriers such as Au–Si (~0.75 eV), Au–TiO_2 (~1 eV), and Au–MoS_2 (~0.5 eV). The HED mechanism involves three steps: the first is photoelectron generation, the second one is the transport of the hot electrons through the dielectric/semiconducting layer, and the final one is the injection of the electron to the opposite metal contact. In the photoelectron generation process, hot electrons are generated at one of the Au contacts, say the top Au contact, *via* the absorption of photons. In this process, electrons are transferred from states below E_f to higher states with the consumption of photon energy. In the second step of carrier transport, about half of the generated hot electrons migrate towards the Au–Sb_2S_3 interface. A fraction of these electrons will reach the interface without losing energy through inelastic collisions. Importantly, hot e^- generated within the diffusion length can only transport to the interface (Au–Sb_2S_3). Some of the hot electrons, arriving at the interface, having kinetic energy larger than the barrier height, ϕ_b, of the Au–Sb_2S_3 interface get injected into the Sb_2S_3 layer. This fraction generally used to be small due to impedance mismatch between the metal and dielectric but can be tuned in the present case through the Amp–Cry phase transition. A small fraction of the electrons get injected into the dielectric region will reach the second Au contact without losing energy through inelastic collisions. This fraction can be also tuned through the Amp to Cry phase transition. Finally, the electrons get injected into the opposite metal electrode, but the density of such electrons depends on the impedance of both regions. The photoresponsivity (R) of the generated hot electrons due to photon absorption within the diffusion length of the metal is given by the Fowler model with the following expression: $R(\omega) = qA(\omega)\eta/\hbar\omega$ and $\eta = (\hbar\omega - \Phi_b)^2/4E_f\hbar\omega$, where $\hbar\omega$ is the energy of the incident photon, A is the absorption, and η is the internal quantum efficiency.[24] Here we concentrate our investigation on the contribution of hot e^- only and we formally verify our calculations with some of the recent literature on HEG in a planar configuration.[17–19]

Fig. 2(a) shows the contrast in the refractive index (Δn) and the extinction coefficient (Δk) of the Sb_2S_3 complex. The Amp phase of Sb_2S_3 shows a higher refractive index than the Cry phase, attaining a maximum difference of $\Delta n \sim 1$ at 614 nm. The imaginary part is zero for wavelengths above 550 nm for the amorphous phase and the amorphous phase is negligible after 750 nm. Fig. 2(b) shows the absorption coefficient as a function of incident photon energy in the Cry and Amp phases. Due to this significant contrast in the index and absorption coefficient, Sb_2S_3 offers dynamic tunability in the proposed PCM-HEPD.

Fig. 3(a) and (b) show the contour plot for reflection as a function of wavelength and h at normal incidence for the Cry and Amp phases, respectively. The thickness h has a great impact on critical light coupling into the cavity or resonance conditions and is given by $2nh = (m + 1/2)\lambda_0$, where n is the refractive index of the cavity, m is the order of mode, and λ_0 is the resonance wavelength. Upon increasing or decreasing h, the number of modes supported by the cavity can be increased or decreased significantly. The FP interference is the governing mechanism of the MDM structure that explains the selective absorption of light. Apart from h, the cavity index n also has a great influence on the resonance conditions. So one can fix the resonance conditions for a given h and n, and this limits the dynamic nature of the MDM cavity. Due to the high index contrast between the Cry and Amp phases, a PCM can be employed to overcome the limitation and offer dynamic tunability in resonance conditions or the absorption band.

Fig. 3(a) and (b) show that on increasing h from 10 nm to 400 nm, higher-order resonance starts appearing. Modes supported typically follow the resonance conditions. The cavity can dynamically control the absorption band and its line width is from 400 nm to 1200 nm. One can wisely choose the parameters discussed and can use the proposed MDM cavity correspondingly for different applications from the visible to NIR region. At resonance, the electric field is strongly confined

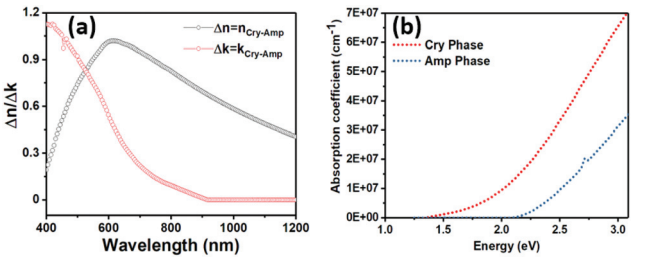

Fig. 2 (a) Index contrast for Sb_2S_3 and (b) absorption coefficient as a function of photon energy in the Cry and Amp phases. Δn and Δk are the difference in the real and imaginary parts of the index between the Cry and Amp phases of Sb_2S_3, respectively.

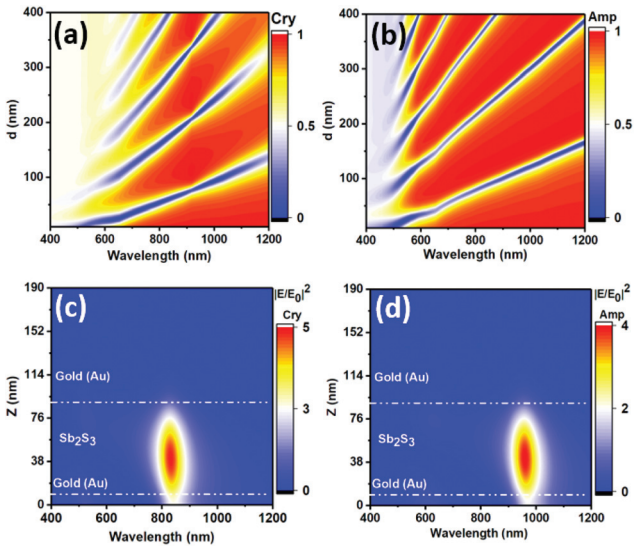

Fig. 3 Absorption as a function of incident wavelength and Sb_2S_3 thickness (h) in the (a) Cry phase and (b) Amp phase. Electric field intensity distribution in different layers of the structure as a function of wavelength (c) in the Cry phase and (d) in the Amp phase for normal incidence with t = 10 nm, h = 80 nm, and H = 100 nm.

into the dielectric layer as a result of constructive interference between the incident and reflected light. Additionally, the electric field intensity distribution profile is shown in Fig. 3(c) and (d) for the Cry (E_Cry) and Amp (E_Amp) phases, respectively, at normal incidence. Two notable field distribution windows are visible: (i) a Beer–Lambert region (B. L. region), in which Sb_2S_3 is absorbing and no field enhancement and (ii) an interference region where the material is not absorbing and light can completely pass the absorbing media and gets reflected from the bottom Au layer.

At resonance, the electric field is strongly confined into the Sb_2S_3 layer as a result of constructive interference between the incident and reflected light from the bottom Au layer in the interference region or after the B–L region. Field distribution has been calculated as a function of wavelength and in the direction of propagation (Z). The electric field is mainly distributed or confined to the middle layer with a narrow band and high enhancement at the resonance wavelength. A clear FP resonance can be seen corresponding to the modes present. The modes switch with the phase transition in Sb_2S_3. In the Cry phase, the enhancement is at ~820 nm, while in the Amp phase it appears at ~1000 nm. However, the electric field enhancement is strong in the Sb_2S_3 layer but absorption is very low due to the negligible imaginary refractive index in the region or below the E_g of Sb_2S_3. Therefore, absorption in the Sb_2S_3 layer does not contribute to the photovoltaic response or the hot e^- detection of the device. Ultimately, the absorption from the Au film is an essential contribution in the hot e^- detection and photoresponsivity. The relationship between the electric field and optical absorption is given by the following expression: $Q = 1/2\omega Im(\varepsilon)|E(z,\omega)|^2$, where Im($\varepsilon$) is the imaginary parts of metal and dielectric permittivities and $|E(z,\omega)|^2$ represents the electric field intensity. Finally, the hot e^-generation rate can be written as $G = Q/\hbar\omega$.[25] The generated hot e^- can be transported to the interface by jumping over the barrier height or through tunneling. It is highly desirable to look into them carefully. The probability of hot carriers to reach the interface after generation without e^- – e^- and e^-–phonon scattering is given by the following expression: $p = 1/2\pi \int_0^{\pi} \exp[(-d/l \sin\theta)]d\theta$, where d and l are the distance of hot-electron generation from the interface and the mean free path (MFP) and θ is a specific angle for each possible path for e^-. For Au, the MFP for a hot electron is 37.7 nm. The probability of hot electrons to reach the interface depends on the MFP and distance of the position of their origin from the interface. The absorption and photoresponsivity of HEPD are significantly affected by varying t and h. Fig. 4 shows a blueshift and a redshift in the absorption and responsivity with an increase in the t and h values, respectively. The value of full-width half maxima (FWHM) decreases from 150 nm to 20 nm with an increase in the t value from 10 at 50 nm. If the metal thickness is more than the skin depth of the EM wave, it leads to a strong reduction in the absorption due to an increment in the impedance mismatch and consequently a lower penetration of light into the metal. The maximum responsivity is ~30 mA W^{-1} at t = 30 nm. The Au diffusion length for hot e^- is ~20 nm, which means that the hot electrons generated within 20 nm thickness of the metal can reach the Au–Sb_2S_3 interface before thermalization. Therefore, we can fix t at 20 nm or less to calculate the responsivity. From resonance conditions, it is well known that the cavity resonance depends on h and n values of the cavity. Therefore, one can wisely select a value for h to achieve the resonance or wavelength of interest for the required application. The Sb_2S_3 cavity provides a dynamically tunable platform *via* coupling into the cavity through the phase transition with external stimuli such as temperature and

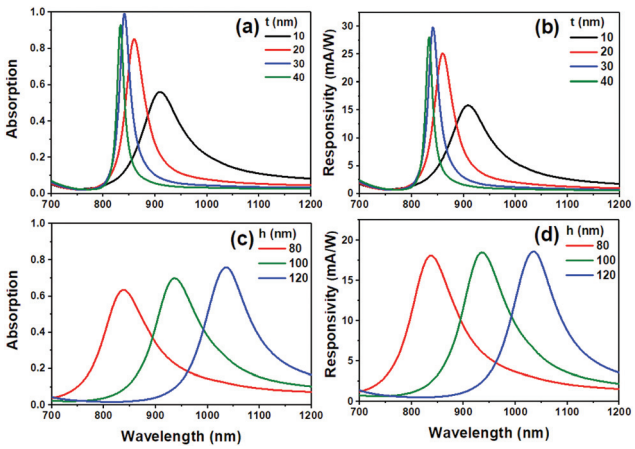

Fig. 4 Absorption and responsivity as a function of wavelength for Amp Sb_2S_3. (a) Absorption and (b) responsivity with varying t at h = 80 nm. (c) Absorption and (d) responsivity with varying h at t = 10 nm and normal incidence.

voltage. It showed a broad range of operation from 600 nm to 1200 nm to detect the generated hot e^-. The absorption response of the Amp Sb_2S_3 cavity for t = 10 nm is shown in Fig. 4(c) with varying h. With an increase in the h value, the absorption spectrum shows a red shift in the resonance peak with broadening of the FWHM. The corresponding responsivity is shown in Fig. 4(d) at t = 10 nm. The optimized value of responsivity is ~18 mA W^{-1}, which is almost invariant with h for the Amp phase of Sb_2S_3. Responsivity not only depends on the total absorption but also on the absorption ratio, metallic film distribution, and critical light coupling or the resonance wavelength of light.

The absorption of photons results in the generation of a hot carrier (e^- – hole) pair. Fig. 5(a) shows the tunability of the generation rate G between the Cry and Amp phases as a function of wavelength. It demonstrates high G at 850 nm in the Cry phase and 1000 nm in the Amp phase with a high FWHM of ~120 nm. It also indicates a high probability for hot carriers to overcome the Au–Sb_2S_3 barrier and reach the interface. Therefore, all the calculations, here, are done for the normal incidence and S-polarized light. The critical coupling conditions into the cavity, however, can be significantly influenced by varying the incidence angle and polarization of light. Fig. 5(b)–(e) show the spectral reflection as a function of incident angle and polarization for 40 nm thick Sb_2S_3. In the Amp phase, a strong absorption band with a FWHM of ~100 nm is present at ~570 nm for both polarizations (see Fig. 5b and c). Upon phase transition to the Cry phase, the band gets red-shifted to ~650 nm with broadening in the bandwidth at ~150 nm in both polarizations (see Fig. 5d and e). This tunability in the absorption band using the ultrathin Sb_2S_3 layer can be very important for many other nanoscale photonics applications. The figure of merit of a photodetector (PD) is its minimum dark current (J_d) and maximum detectivity (D). Therefore, it is important to know the J_d and D of the HEPD for its full characterization. The J_d and D of the proposed HEPD device can be given by the following thermionic emission expressions (considering the negligible or weak biasing voltage): $J_d = AT^2 \exp(-q\Phi_b/kT)$ and $D = R/\sqrt{2qj_d}$.[17] Here $A = 4\pi qmek^2/h^3$ is the Richardson constant, q is the elementary charge, k is the Boltzmann constant, h is Planck's constant, and m_e is the effective mass ($m_e \sim 1.035m_0$ for Sb_2S_3 and m_0 is the e^- mass in free space). A is ~125A (cm^2 K^{-2})$^{-1}$ for Sb_2S_3 at room temperature (300 K). The estimated J_d and D in the Cry phase are 4.21 × 10^{-10} A cm^{-2} and 5 × 10^{12} cm $Hz^{1/2}$ W^{-1} (jones), respectively at 700 nm. In the Amp phase at 700 nm, J_d and D were calculated to be 15 A cm^{-2} and 1.9 × 10^6 cm $Hz^{1/2}$ W^{-1} (jones), respectively. Detectivity is the detection capability of a PD device to detect a weak light signal. Due to the negative exponential correlation between J_d and Φ_b, an increase in the Φ_b results in a reduction in J_d and R, but an increase in D. Therefore, careful optimization is required to achieve a high value of D. The responsivity (R), dark current (J_d), and detectivity (D) of the proposed PCM based MDM HEPD are better than or comparable to those of the previously proposed design and can be seen in Table 1 of ref. 26.

Additionally, the responsivity of the proposed HEPD device can be increased effectively by forming a double cavity, known as the hybrid double cavity system (hereafter), as shown in Fig. 6(a). There are four possible combinations to arrange the hybrid double cavity as follows: Amp–Amp, Amp–Cry, Cry–Cry, and Cry–Amp. Phase accumulation (ψ) in the cavity can be written as $\psi = Y_1 + Y_2 + 2nh$, where Y_1 and Y_2 are the phase shift at the top Au/top Sb_2S_3 and top Sb_2S_3 and bottom Au. 2 nh is the phase accumulation due to the round trip in the top Sb_2S_3 layer. The same conditions can be written for the second cavity. Perfect absorption occurs, once the phase accumulation satisfies the FP resonance conditions. The upper MDM cavity acts as a transmission filter and coupling medium between two cavities. Depending on the cavity parameters, it provides multiple perfect absorption bands. Fig. 6(b) and (c) show a comparison of the absorption response and responsivity respectively between the Amp single and double cavity. The

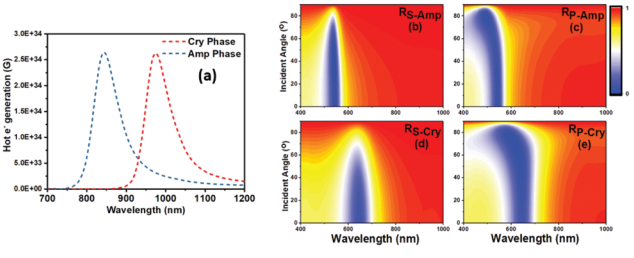

Fig. 5 (a) Tunability in the hot electron generation rate in the Cry and Amp phases. t = 10 nm, h = 80 nm, H = 100 nm, and normally incident light. Angular and polarization dependent reflection in the Cry and Amp phases, (b) S – polarized light – Amp, (c) P – polarized light – Amp, (d) S – polarized light – Cry, and (e) P – polarized light – Cry. t = 15 nm, h = 40 nm, and H = 100 nm.

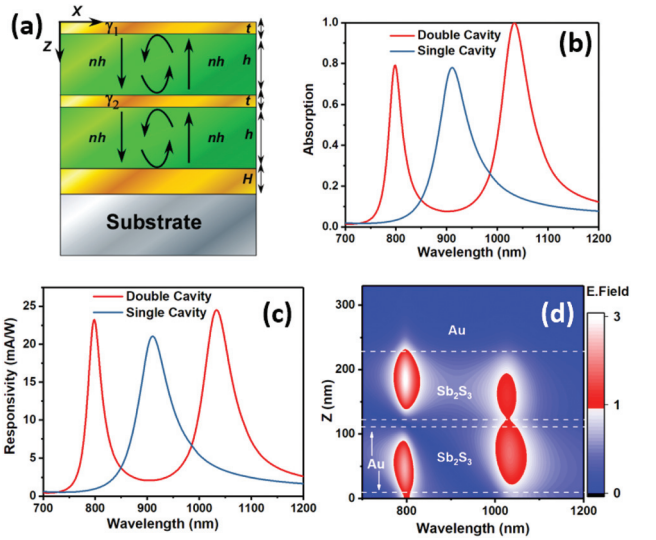

Fig. 6 (a) A schematic of the proposed double cavity. Absorption (b) and responsivity (c) comparison between the single and double cavities. (d) Electric field distribution as a function of wavelength and location in the double cavity. t = 15 nm, h = 100 nm, and H = 100 nm.

double cavity shows two bands at 800 nm with 80% absorption and at 1000 nm with ~100% absorption. The electric field of the HEPD with double cavities as a function of wavelength and depth direction is shown in Fig. 6(d). The electric field distribution further shows the presence of symmetric and antisymmetric modes at a lower wavelength of 800 nm and a higher wavelength of 1033 nm, respectively. However, the electric field is essentially confined more in the top cavity at a low wavelength, although it is confined in the bottom cavity at a longer wavelength resonance. The resonance at a long wavelength provides high absorption to the middle Au layer which further enhances the responsivity.

Furthermore, the double cavity enhances the overall responsivity with a maximum value of 23 mA W^{-1} and 24.58 mA W^{-1} at 800 nm and 1033 nm, respectively. In the double cavity configuration, the thickness values of the upper and lower cavities determine the value of responsivity in the present symmetric and antisymmetric modes. For example, an equal cavity thickness results in almost the same responsivity. If the upper cavity is thicker or thinner than the lower cavity, the corresponding response will be higher or lower. Table 1 shows a comparison in terms of the barrier height and maximum responsivity of the proposed PCM based HEPD with previously proposed planar HEPDs.[27,28]

Apart from Sb_2S_3, other PCMs such as $Ge_2Sb_2Te_5$ (GST) and vanadium dioxide (VO_2) can be a good choice for hot electron detection in a planar configuration. The bandgap and electron affinity of Cry-GST and Amp-GST are (0.7 eV, 0.38 eV) and (0.5 eV, 0.08 eV), respectively.[29] Accordingly, the Ag-GST Schottky junction provides the HEPD range for Cry-GST as 2479.694 nm < λ < 15 498.1 nm and for Amp-GST as 1771.21 nm < λ < 3262 nm. The estimated barrier height for GST in its Amp and Cry phases with Ag is 0.38 eV and 0.08 eV, respectively. This is again the lowest among all the mentioned material choices for the planar HEPD. VO_2 is a promising material for optically active devices. It shows a semiconductor (SC)-to-metal (M) phase transition at 68 °C. It shows a work function of ~5.15 eV in the insulating phase and increases by ~0.15 eV upon phase transition to a metal.[30] The phase transition in VO_2 can be exploited as switching from the single to double cavity. In the metallic phase, VO_2 can work as a coupling medium for a double cavity and upon phase transition to a semiconductor single cavity. VO_2-SC has an E_g of 0.6 eV and a Φ_b of 0.3 eV with Au.[28] MoS_2 has been integrated as a cavity material due to its amazing semiconducting nature and high index. Bulk MoS_2 has an indirect bandgap of 1.3 eV. The calculated barrier height between the VO_2–M–MoS_2 and Au–MoS_2 interfaces is 0.7 eV and 0.5 eV, respectively. So the estimated HED range is 953 nm < λ < 1771.2 nm and 953 nm < λ < 2480 nm at the VO_2–MoS_2 and Au–MoS_2 junction, respectively. Moreover, VO_2 shows a phase transition at the femtosecond time scale and can be tuned *via* optical or magnetic excitation, electrically and thermally.[31,32]

Table 1 A comparison of the barrier height (Φ_b) and responsivity (R) between the proposed PCM based HEPD and a few previously reported planar single cavity HEPDs

Planar structure	Φ_b (eV)	Max R (mA W^{-1})	Ref.
Au–TiO_2/Au	1	0.66	18
Au-n–Si/Au	0.8	1.72	17
Au–MoS_2/Au	0.5	15.6	19
Au–Amp–Sb_2S_3–Au	0.35	20	Our work

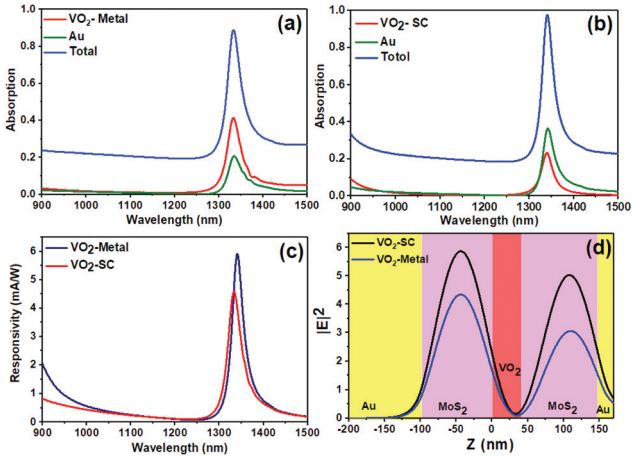

Fig. 7 Absorption in top Au, middle coupling layer VO_2, and total absorption (a) when VO_2 in the metal phase, (b) when VO_2 in the SC phase, (c) responsivity of the double cavity formed with VO_2 as the metal and SC, and (d) electric field distribution in different layers of the double cavity in SC and metal phases of VO_2.

Fig. 7(a) and (b) show absorption in the top Au, VO_2, and total absorption by the double cavity. One can see high absorption in the metal phase of VO_2 (see Fig. 7(b)). Correspondingly, the responsivity in the VO_2 metal double cavity is 50% higher than VO_2–SC (see Fig. 7(c)). Electric field distribution as a function of location in the device is shown in Fig. 7(d). The field intensity in VO_2–SC is higher due to less absorption. So, upon phase transition, PCMs (Sb_2S_3, VO_2, and GST) show a significant difference in their ϕ_b, E_g, and refractive index, which provides large tunability in terms of responsivity in the spectral wavelength range. This makes them important materials for actively tunable optical devices with great promise for HEPDs in the planar configuration. PCMs can also be employed for many other applications including optoelectronics, optical gating, and tunable spontaneous emission rate.[33]

Conclusions

In summary, we have numerically demonstrated the integration of a PCM for a planar tunable HEPD. The phase transition in the cavity offers a broad range of operation for photodetection particularly in the NIR region with a broad FWHM. Depending upon the thickness of Sb_2S_3, the cavity can support multiple absorption bands. The minimum cavity thickness which supports the critical coupling of light is ~40 nm. Due to the low barrier height of Au–Sb_2S_3, the photoresponsivity of

the PCM-based HEPD is higher than previously proposed HEPDs in the planar configuration. The maximum predicted photoresponsivity is 20 mA W^{-1} in a single cavity, and employing a double cavity enhanced the responsivity of ~24.58 mA W^{-1} which has been observed with one perfect absorption band at a higher wavelength. The calculated J_d and D in the Amp and Cry phases are 4.21×10^{-10} A cm^{-2} and 5×10^{12} jones @ 700 nm and 15 A cm^{-2} and 1.9×10^6 jones @ 700 nm, respectively. So Amp Sb_2S_3 shows minimum dark current and maximum detectivity. Eventually using another PCM called VO_2 we have demonstrated switching in the coupling between the top and bottom cavities by exploiting the SC to metal phase transition in VO_2. Upon phase transition from the SC to a metal, 50% enhancement has been observed in responsivity. The proposed HEPD possesses the advantages of being low cost, easy to fabricate, and scalable as it provides a lithography free platform. It can also be used in many other applications such as sensing, filtering, other photovoltaic applications, solar cells, and spectroscopy. Moreover, it can be a better candidate than Tamm plasmon based HEPDs in terms of nanoscale thickness.

Conflicts of interest

There are no conflicts to declare.

Acknowledgements

S. K. C. gratefully acknowledges his sponsorship by "CAS-TWAS" Presidential Fellowship for international doctorate students. We also would like to thank following funding sources: National Natural Science Foundation of China (NSFC) (91750205, 61774155, 51102107), The 863 Program (2013AA014402) and K. C. Wong Education Foundation (GJTD-2018-08).

References

1 V. M. Shalaev, C. Douketis, J. T. Stuckless and M. Moskovits, *Phys. Rev. B: Condens. Matter Mater. Phys.*, 1996, **53**, 11388.
2 W. C. Brown, *IEEE Trans. Microwave Theory Tech.*, 1984, **MIT-32**, 1230.
3 W. Li, Z. L. Coppens, L. V. Besteiro, W. Wang, A. O. Govorov and J. Valentine, *Nat. Commun.*, 2015, **6**, 8379.
4 M. W. Knight, H. Sobhani, P. Nordlander and N. J. Halas, *Science*, 2011, **332**, 702.
5 C. Clavero, *Nat. Photonics*, 2014, **8**, 95.
6 M. Taghinejad, H. Taghinejad, Z. Xu, Y. Liu, S. P. Rodrigues, K.-T. Lee, T. Lian, A. Adibi and W. Cai, *Adv. Mater.*, 2018, **30**, 1704915.
7 P. J. Schuck, *Nat. Nanotechnol.*, 2013, **8**, 799.
8 S. Linic, P. Christopher and D. B. Ingram, *Nat. Mater.*, 2011, **10**, 911.
9 M. W. Knight, Y. Wang, A. S. Urban, A. Sobhani, B. Y. Zheng, P. Nordlander and N. J. Halas, *Nano Lett.*, 2013, **13**, 1687–1692.
10 J. Hou, H. Zhu, J. C. Reed, F. Yi, E. Cubukcu and D. A. Bonnell, *Appl. Phys. Lett.*, 2017, **110**, 043103.
11 A. Pescaglini, A. Martín, D. Cammi, G. Juska, C. Ronning, E. Pelucchi and D. Iacopino, *Nano Lett.*, 2014, **14**, 6202–6209.
12 B. Desiatov, I. Goykhman, N. Mazurski, J. Shappir, J. B. Khurgin and U. Levy, *Optica*, 2015, **2**, 335–338.
13 B. Jeon, H. Lee, K. C. Goddeti and J. Y. Park, *ACS Appl. Mater. Interfaces*, 2019, **11**(16), 15152–15159.
14 Y. Park, J. Choi, C. Lee, A. Cho, D. W. Cho, N. Park, H. Ihee and J. Y. Park, *Nano Lett.*, 2019, **19**(8), 5489–5495.
15 W. Li, Z. J. Coppens, L. V. Besteiro, W. Wang, A. O. Govorov and J. Valentine, *Nat. Commun.*, 2015, **6**, 8379.
16 W. Li and J. Valentine, *Nano Lett.*, 2014, **14**, 3510.
17 W. Long, C. Yifu, Li Liang and Q. Chen, *ACS Photonics*, 2018, **5**, 581.
18 C. Zhang, K. Wu, V. Giannini and X. Li, *ACS Nano*, 2017, **11**, 1719.
19 W. Shao, Q. Yang, C. Zhang, S. Wu and X. Li, *Nanoscale*, 2019, **11**, 1396.
20 S. C. Singh, Y. Peng, J. Rutledge and C. Guo, *ACS Appl. Electron. Mater.*, 2019, **1**(7), 1169–1178.
21 B. Wang, Y. Zou, H. Lu, W. Kong, S. C. Singh and C. Zhao, *Small*, 2020, 2001417.
22 S. Ishii, S. L. Shinde, W. Jevasuwan, N. Fukata and T. Nagao, *ACS Photonics*, 2016, **3**, 1552–1557.
23 W. Dong, *et al.*, *Adv. Funct. Mater.*, 2018, **29**, 1806181.
24 K. Wu, J. Chen, J. R. McBride and T. Lian, *Science*, 2015, **349**, 632.
25 C. Zhang, G. Cao, S. Wu, W. Shao, V. Giannini, S. A. Maier and X. Li, *Nano Energy*, 2019, **55**, 164.
26 Q. Sun, C. Zhang, W. Shao and X. Li, *ACS Omega*, 2019, **4**, 6020.
27 C. Zhang, K. Wu, Y. Zhan, V. Giannini and X. Li, *Nanoscale*, 2016, **8**, 10323.
28 Y. Zhu, *et al.*, *Nanotechnology*, 2020, **31**, 274001.
29 H. Tong, Z. Yang, N. N. Yu, L. J. Zhou and X. S. Miao, *Appl. Phys. Lett.*, 2015, **107**, 082101.
30 K. Changhyun, Y. Zheng and R. Shriram, *ACS Appl. Mater. Interfaces*, 2011, **3**(9), 3396.
31 N. Oliva, E. A. Casu, C. Yan, *et al.*, *Sci. Rep.*, 2017, **7**, 14250.
32 K. Appavoo, B. Wang, N. F. Brady, M. Seo, J. Nag, R. P. Prasankumar, D. J. Hilton, S. T. Pantelides and R. F. Haglund Jr., *Nano Lett.*, 2014, **14**, 1127.
33 S. K. Chamoli, M. ElKabbash, J. Zhang and C. Guo, *Opt. Lett.*, 2020, **45**, 1671.